

Segmentation-Aware Generative Reinforcement Network (GRN) for Tissue Layer Segmentation in 3-D Ultrasound Images for Chronic Low-back Pain (cLBP) Assessment

Zixue Zeng, Xiaoyan Zhao, Matthew Cartier, Tong Yu, Jing Wang, Xin Meng, Zhiyu Sheng, Maryam Satarpour, John M Cormack, Allison Bean, Ryan Nussbaum, Maya Maurer, Emily Landis-Walkenhorst, Dinesh Kumbhare, Kang Kim, Ajay Wasan, Jiantao Pu

Abstract—We introduce a novel segmentation-aware joint training framework called generative reinforcement network (GRN) that integrates segmentation loss feedback to optimize both image generation and segmentation performance in a single stage. An image enhancement technique called segmentation-guided enhancement (SGE) is also developed, where the generator produces images tailored specifically for the segmentation model. Two variants of GRN were also developed, including GRN for sample-efficient learning (GRN-SEL) and GRN for semi-supervised learning (GRN-SSL). GRN's performance was evaluated using a dataset of 69 fully annotated 3D ultrasound scans from 29 subjects. The annotations included six anatomical structures: dermis, superficial fat, superficial fascial membrane (SFM), deep fat, deep fascial membrane (DFM), and muscle. Our results show that GRN-SEL with SGE reduces labeling efforts by up to 70% while achieving a 1.98% improvement in the Dice Similarity Coefficient (DSC) compared to models trained on fully labeled datasets. GRN-SEL alone reduces labeling efforts by 60%, GRN-SSL with SGE decreases labeling requirements by 70%, and GRN-SSL alone by 60%, all while

maintaining performance comparable to fully supervised models. These findings suggest the effectiveness of the GRN framework in optimizing segmentation performance with significantly less labeled data, offering a scalable and efficient solution for ultrasound image analysis and reducing the burdens associated with data annotation.

Index Terms—Image Segmentation, Ultrasound Imaging, Chronic Lower Back Pain, Generative Adversarial Network.

I. INTRODUCTION

CHRONIC lower back pain (cLBP) is a complex and multifaceted condition [1]. It is highly prevalent, with 70-85% of individuals experiencing lower back pain (LBP) at some point in their lives [2]. Additionally, 19.6% of people aged between 20 and 59 report LBP [3, 4], significantly affecting their quality of life [5]. Despite extensive research, etiology-based diagnosis and successful management of cLBP remain elusive, with no consensus on the most effective approaches [6].

Various clinical imaging techniques, including ultrasound, computed tomography (CT), and magnetic resonance imaging (MRI), have been employed to explore the underlying classification and mechanisms of cLBP. CT provides high-resolution cross-sectional images, offering detailed visualization of various anatomical structures, including the vertebrae and muscles [7-9]. However, CT imaging exposes patients to ionizing radiation, which carries potential long-term health risks. Also, it has limited ability to differentiate between soft tissues, making it less effective for detailed assessment of muscular structures [10]. MRI is a non-invasive diagnostic tool that uses powerful magnetic fields and radio waves to produce high-resolution images, particularly suited for visualizing soft tissues, organs, and nervous systems [11, 12]. However, MRI imaging is generally more expensive, less accessible, and time-consuming compared to other imaging methods, limiting its use. By comparison, ultrasound imaging offers a cost- and time-effective alternative without the risks associated with ionizing radiation, making it a valuable and widely used tool in clinical practice for assessing cLBP.

Current ultrasound research on cLBP employs predominantly two-dimensional (2-D) ultrasound imaging to assess muscle thickness, contraction, and tissue echogenicity, which are believed to be associated with LBP [13]. This 2-D imaging approach overlooks volumetric and intricate anatomical structures and thus limits the comprehensiveness of the analysis [14]. In contrast, three-dimensional (3-D) ultrasound imaging offers improved spatial visualization, enabling a more detailed and accurate layer-by-layer analysis from the dermis to the

This work is supported in part by research grants from the National Institutes of Health (NIH) (R61AT012282, R01HL174570 and R01CA237277).

Zixue Zeng is with the Department of Bioengineering and Department of radiology, University of Pittsburgh, Pittsburgh, PA 15213, USA (email: ziz185@pitt.edu)

Xiaoyan Zhao, Tong Yu, Jing Wang, Xin Meng, and Maryam Satarpour are with Department of Bioengineering, University of Pittsburgh, Pittsburgh, PA 15213 USA (email: XIZ318@pitt.edu; TOY25@pitt.edu; JIW346@pitt.edu; mengx01@gmail.com; MAS1338@pitt.edu).

Matthew Cartier is with Department of Mathematics, University of Pittsburgh, Pittsburgh, PA 15213, USA (email: MAC940@pitt.edu).

Zhiyu Sheng and John M Cormack are with Department of Medicine, University of Pittsburgh, Pittsburgh, PA 15213, USA (email: ZHS41@pitt.edu; JMC345@pitt.edu).

Allison Bean and Ryan Nussbaum are with Department of Physical Medicine and Rehabilitation, University of Pittsburgh, Pittsburgh, PA 15213, USA (email: BEANAC2@pitt.edu; NUSSBAU@pitt.edu).

Maya Maurer, Emily Landis-Walkenhorst, and Ajay Wasan are with School of Medicine, University of Pittsburgh, Pittsburgh, PA 15213, USA (email: MAM708@pitt.edu; EMW235@pitt.edu; wasanad@upmc.edu).

Dinesh Kumbhare is with Department of Medicine, Division of Physical Medicine and Rehabilitation, University of Toronto, Toronto, Ontario M5S3H2, Canada (email: Dinesh.Kumbhare@uhn.ca).

Kang Kim is with Department of Bioengineering and Department of Medicine, University of Pittsburgh, Pittsburgh, PA 15213, USA (email: kangkim@pitt.edu).

Jiantao Pu is with Department of Bioengineering, Department of Radiology and Department of Ophthalmology, University of Pittsburgh, Pittsburgh, PA 15213, USA (email: jip13@pitt.edu)

muscle. This comprehensive volumetric data allows for the identification of subtle morphological changes and the assessment of tissue interactions, making 3-D ultrasound a superior modality for studying cLBP. However, each 3-D scan can produce hundreds of image slices, making manual annotation extremely labor-intensive and limiting the availability of annotated data necessary for training robust deep learning models. Also, this technique may be constrained by limited penetration depth and is prone to artifacts and noise, which can compromise image quality[15]. Furthermore, existing studies typically focus on a limited number of tissues rather than performing a comprehensive layer-by-layer analysis from the dermis to the muscle. Consequently, essential information regarding individual tissues and their interactions across layers might be omitted. Therefore, an automated layer-by-layer segmentation solution would be highly valuable for identifying image biomarkers associated with cLBP from 3-D ultrasound imaging data.

Several advanced machine learning techniques are being explored to address the challenge of training AI modes with limited annotated data, such as few-shot learning[16], sample-efficient learning (SEL), Semi-supervised learning (SSL)[17], and Generative Adversarial Networks (GANs) [18]. Few-shot learning emphasizes rapid generalization to new tasks rather than improving performance on existing tasks with limited data. In contrast, SEL aims to maximize model performance while minimizing training examples. A common SEL strategy is data augmentation [19]. Some investigators have advocated for augmentation methods that generate challenging examples by maintaining an adversarial relationship with downstream models to minimize task-specific losses to enhance robustness [20]. Others focus on minimizing task-specific losses by optimizing augmentations to produce denoised samples and thus improve performance [21]. However, limited research has explored the potential of developing a more comprehensive augmentation framework that generates both challenging and denoised samples. SSL combines supervised training on a limited amount of labeled data with unsupervised training on a larger pool of unlabeled data to enhance performance and generalization [17, 22-26]. However, SSL depends on high-quality labeled data and is based on key assumptions, such as smoothness (similar data points yield similar predictions) and clustering (data naturally forms distinct and well-defined groups), which may not always be valid in real-world scenarios. GAN has been widely used to generate synthetic images to augment data [27-30]. However, GAN-based augmentation typically requires pre-training the model to generate synthetic images. These images may not accurately replicate real-world images and do not always lead to improved performance for segmentation models [31].

In this study, we propose an innovative framework termed generative reinforcement network (GRN). GRN integrates generative and segmentation models (segmentor) through a collaborative learning loop. Unlike traditional data augmentation techniques, GRN establishes a feedback mechanism where the segmentation model actively guides the generator during each training iteration via back-propagated losses. This design ensures that the generator produces denoised augmented images specifically optimized to improve segmentation performance. Additionally, interpolation

consistency training is employed to generate challenging samples to enhance the model’s robustness when applied to unseen data. During inference, the generator also functions as an image enhancement tool for preprocessing inputs by emphasizing features critical for segmentation, thereby improving the reliability of tissue segmentation. GRN supports both SEL and SSL scenarios. By reducing the dependence on extensive manual labeling, it achieves competitive and often superior performance compared to fully supervised models. This efficiency makes GRN particularly effective for problems like ours, namely tissue layer segmentation in 3-D ultrasound imaging.

II. MATERIALS AND METHODS

A. Study Dataset

The dataset is acquired from an ongoing project funded by the National Institute of Health (NIH), which enrolls participants with cLBP and healthy controls (Institutional Review Board: STUDY22090014). All participants were positioned face-down on an examination table. The ultrasound array transducer was placed laterally to the midline at the lumbar 3-4 (L3-L4) vertebral interspace (Fig. 1, Part 1), specifically targeting the multifidus (MF) and erector spinae (ES) muscles. A row-column array (RCA) transducer (RC6gV, Vermon), operating at a center frequency of 6 MHz with an active aperture of 25.6 mm \times 25.6 mm, was connected to the Vantage 256 ultrasound system (Verasonics Inc., WA, USA) to acquire 3-D volumetric ultrasound data. A synthetic aperture technique was used during acquisition to improve image quality. To acquire a single frame, each element of the transducer individually transmits one pulse in sequence until all the elements have performed transmissions, and after each transmission, all the elements simultaneously receive the echo signals. This enabled a synthetic aperture (SA) approach to achieve dynamic focusing during beamforming for image reconstruction.

Temporal compounding was applied by averaging three consecutive frames to improve the image signal-to-noise ratio. Both the right and left sides of the back were scanned. On each side, two specific locations over the MF and ES muscles were targeted by experienced ultrasound examiners (with 9 (ACB) and 25 (ADW) years of clinical experience). Each designated location was scanned three times, yielding a total of 12 B-mode scans per participant. A total of 29 participants were enrolled and used for this study. We randomly sampled 69 scans ($N_{image} = 17,664$) taken from various locations across 29 patients for algorithm development (Table I). An experienced ultrasound operator (Ms. Zhao) meticulously annotated six distinct anatomical layers depicted on the 3-D ultrasound scans, including the dermis, superficial fat, superficial fascial membrane (SFM), deep fat, deep fascial membrane (DFM), and MF muscle (Figure 1, Parts 2 & 3). For the purpose of deep learning model training, the annotated B-mode images were divided into training ($N_{image} = 10,722, N_{scan} = 44, N_{patient} = 16$), internal validation ($N_{image} = 512, N_{scan} = 2, N_{patient} = 2$), and independent test ($N_{image} = 6,430, N_{scan} = 23, N_{patient} = 11$) sets at the patient level. To ensure a more reliable estimate of model performance, we set aside a

relatively larger independent test set comprising 23 scans from different patients.

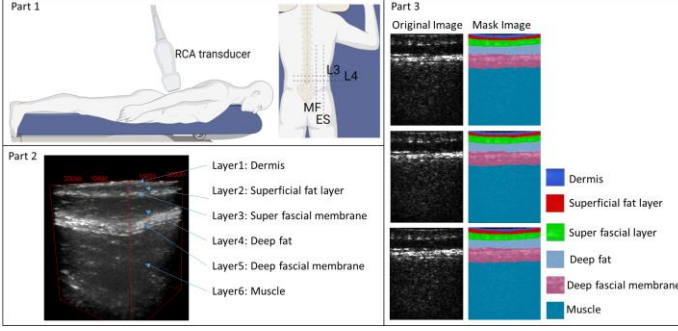


Fig. 1. 3-D ultrasound B-mode image acquisition and annotations. Part 1: ultrasound image acquisition. Part 2: A 3-D ultrasound B-mode image depicting six tissue layers. Part 3: Original B-mode images along the coronal or sagittal directions paired with their corresponding annotations, where each color represents a specific tissue layer.

Table I
DESCRIPTIVE STATISTICS INFORMATION FOR DEMOGRAPHIC VARIABLES AND LBP STATUS

N = 29	Summary
Demographic variable	
Age	47.11 (19.34)
Female	18 (62.07%)
Hispanic or Latino	1 (3.44%)
African American	2 (6.90%)
Non-Hispanic White	26 (89.65%)
Height (in inches)	66.38 (3.80)
Weight(in pounds)	179.83 (36.02)
LBP status	
Positive	21 (72.41%)

Summary statistics are reported as mean (standard deviation) for continuous measurements and number of individuals (percentages) for categorical measurements.

B. Generative Reinforcement Network (GRN)

GRN is designed to generate both challenging interpolated samples and denoised samples to improve segmentation model performance (Fig. 2.). Within this framework, we introduce two variants: **GRN-SEL** for sample-efficient learning and **GRN-SSL** for semi-supervised learning. In GRN-SEL, the generator G reconstructs the original image, which is then passed through the segmentor. Similar to smart augmentation, we utilize a feedback mechanism where the segmentor provides feedback to the generator via the segmentor loss during each training iteration [21]. This feedback mechanism allows the generator to create images tailored to denoise the original input and generate reconstructed images. This approach, termed segmentation-aware denoising augmentation, optimizes the following objective function:

$$\min_G \left(\min_S L_{seg}(S(G(x)), y) \right), \text{ where } x \sim p_{data}(x) \quad (1)$$

where x is sampled from the prior distribution $p_{data}(x)$, and y represents the ground truth. G and S denote the generator and segmentor, respectively. L_{seg} is the segmentor's loss. To further enhance model performance, GRN-SSL incorporates interpolation consistency training, which generates challenging interpolated samples that lie outside the original training data distribution. Training the model on these interpolated samples exposes it to a broader variety of data, significantly improving robustness and enabling better generalization to unseen data.

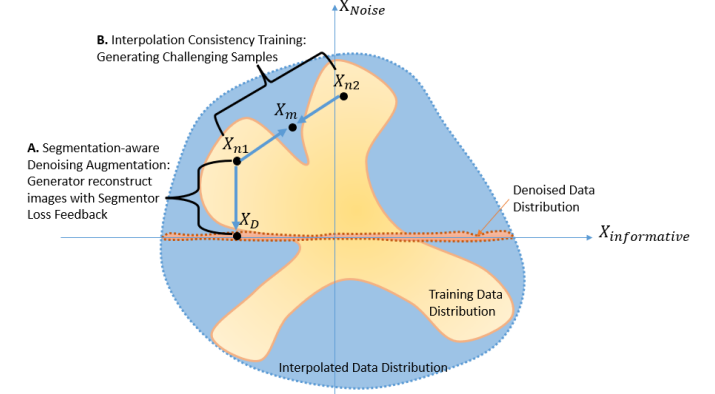


Fig. 2. Illustration of GRN-based data augmentation. The dotted outline shows the augmented dataset distribution, while the solid outline depicts the non-augmented dataset. In the segmentation-aware denoising augmentation, samples are denoised with X_{Noise} close to 0.

1) Sample-efficient and Semi-supervised Generative Reinforcement Network

GRN-SEL combines a GAN model with the segmentor feedback mechanism (Fig. 3). In each training iteration, the generator G_θ processes each labeled image to produce a reconstructed version. The segmentor $S_{\theta''}$ then generated predicted masks from those reconstructed images. A Dice loss is calculated based on the difference between these predicted masks and the ground truth masks, and the loss is backpropagated to the generator. This feedback encourages G_θ to refine its reconstruction by removing noise and irrelevant details, enabling the segmentor to focus on important features and thereby improving robustness.

Like a traditional GAN model, the generator G_θ also receives feedback from the discriminator $D_{\theta'}$, which classifies each reconstructed image as real or fake. Additionally, the segmentor processes both original, unaltered images and the reconstructed images and calculates a combined Dice loss based on mask prediction from both. This dual-processing approach promotes the segmentation model's robustness and stability by ensuring consistent performance on both generator-processed and original images. The comprehensive loss functions are defined as follows:

$$L_G = \lambda_{adv} L_{MSE}(D_{\theta'}(\hat{I}_L), 1) + \lambda_{seg} L_{Dice}(\hat{M}_L, M) + \lambda_{L1} L1(\hat{I}_L, I_L) \quad (2)$$

$$L_S = \frac{L_{Dice}(M_L, M) + L_{Dice}(\hat{M}_L, M)}{2} \quad (3)$$

$$L_D = \frac{L_{MSE}(D_{\theta'}(I_L), 1) + L_{MSE}(D_{\theta'}(\hat{I}_L), 0)}{2} \quad (4)$$

// 1: Real, 0: Fake

where L_{MSE} represents the Mean Squared Error (MSE) loss. L_{Dice} represents the Dice loss and L1 represents the L1 loss. λ_{adv} , weights λ_{seg} and λ_{L1} control the contributions to each loss component. I_L and \hat{I}_L are the labeled image and its reconstructed version. M is the ground truth mask. M_L and \hat{M}_L are the mask prediction for the labeled image and reconstructed image, respectively. The generator loss function combines both generator and discriminator feedback loss terms, ensuring image generation supports not only realism but also effective learning by the segmentor.

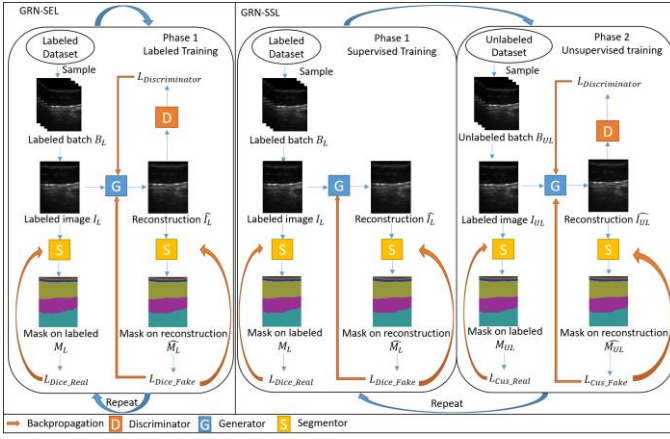


Fig. 3. Architectures of GRN-SEL and GRN-SSL. In GRN-SEL the generator receives feedback from the segmentor through backpropagation of the segmentation loss L_{Dice_Fake} . GRN-SSL operates in two phases: Phase 1 (supervised training) and phase 2 (unsupervised training) with batches of equal size sampled from each dataset to ensure balanced contributions from labeled data and unlabeled data. The GRN-SSL architecture is similar to that of GRN-SEL, except that during the unsupervised training phase, a customized loss that evaluates model prediction on unlabeled images is back-propagated to the generator.

GRN-SSL extends the segmentor feedback mechanism to the unlabeled training process by replacing the segmentation loss with a customized loss that evaluates segmentation model consistency (i.e., interpolation consistency loss in this study) (Fig. 3). A two-phase alternate-batch strategy is implemented to balance labeled and unlabeled datasets. In each iteration, a labeled B_L and an unlabeled batch B_{UL} are sampled from the labeled dataset $Dataset_L(I, M)$ and the unlabeled dataset $Dataset_{UL}(I, M)$, respectively. The training process includes two phases for each iteration, a supervised training phase with B_L and an unsupervised training phase with B_{UL} . The supervised training phase mirrors the process in GRN-SEL, except that discriminator training is moved to the unsupervised training phase. Since $Dataset_{UL}(I, M)$ contains significantly more images than $Dataset_L(I, M)$, including the discriminator in the unsupervised training is sufficient to enhance model robustness. The loss functions are as follows:

$$L_G = \lambda_{seg} L_{Dice}(\widehat{M}_L, M) + \lambda_{L1} L1(\widehat{I}_L, I_L) \quad (5)$$

$$L_S = \frac{L_{Dice}(M_L, M) + L_{Dice}(\widehat{M}_L, M)}{2} \quad (6)$$

In the unsupervised training phase, the generator processes unlabeled images to produce reconstructed versions, and the segmentor generates the corresponding masks. Instead of using traditional segmentation loss like GRN-SEL, a customized consistency loss $L_{customize}$ is defined and back-propagated to the generator. The customized consistency loss can be any predefined loss function used to evaluate model robustness. In this study, we specifically use interpolation consistency loss. As in GRN-SEL, the discriminator evaluates the realism of the generated images and provides feedback to guide image generation. The overall loss function for phase 2 is defined as follows:

$$L_G = \lambda_{adv} L_{MSE}(D_{\theta'}(\widehat{I}_{UL}), 1) + \lambda_{cus} L_{customize}(\widehat{M}_{UL}, M) + \lambda_{L1} L1(\widehat{I}_{UL}, I_{UL}) \quad (7)$$

$$L_S = \frac{L_{customize}(\widehat{M}_{UL}) + L_{customize}(M_{UL})}{2} \quad (8)$$

$$L_D = \frac{L_{MSE}(D_{\theta'}(I_{UL}), 1) + L_{MSE}(D_{\theta'}(\widehat{I}_{UL}), 0)}{2} \quad (9)$$

// 1: Real, 0: Fake

where I_{UL} and \widehat{I}_{UL} represent the unlabeled image and its reconstructed version, respectively M is the ground truth mask. M_{UL} and \widehat{M}_{UL} denote the mask predictions for the unlabeled image and the reconstructed unlabeled image, respectively. Note that the gradients of L_{Dice} in GRN-SEL and $L_{customize}$ in GRN-SSL are passed through generator G and segmentor S simultaneously to enable mutual influence and enhance each other's performance during each training iteration.

Algorithm 1 The Generative Reinforcement Network (GRN) Algorithm for sample-efficient learning

Require: G_{θ} : Generator with trainable parameters θ

Require: $D_{\theta'}$: Discriminator with trainable parameters θ'

Require: $S_{\theta''}$: Segmentor with trainable parameters θ''

Require: $Dataset_L(I, M)$: Collection of labeled samples

Require: T : total number of iterations

for $t = 1, \dots, T$ **do**

Sample $I_L, M \sim Dataset_L(I, M)$

$\widehat{I}_L = G_{\theta}(I_L)$

$P_L = D_{\theta'}(I_L)$

$\widehat{P}_L = D_{\theta'}(\widehat{I}_L)$

$L_D = (L_{MSE}(P_L, 1) + L_{MSE}(\widehat{P}_L, 0))/2$ // 1:Real, 0: Fake

Update θ' based on L_D

$\widehat{M}_L = S_{\theta''}(\widehat{I}_L)$

$L_G = \lambda_{adv} L_{MSE}(\widehat{P}_L, 1) + \lambda_{seg} L_{Dice}(\widehat{M}_L, M_L) + \lambda_{L1} L1(\widehat{I}_L, I_L)$ //

1:Real, 0: Fake

Update θ based on L_G

$M_L = S_{\theta''}(I_L)$

$L_S = (L_{Dice}(M_L, M), L_{Dice}(\widehat{M}_L, M))/2$

Update θ'' based on L_S

end for

return $\theta, \theta', \theta''$

Algorithm 2 The Generative Reinforcement Network (GRN) Algorithm for semi-supervised learning

Require: G_{θ} : Generator with trainable parameters θ

Require: $D_{\theta'}$: Discriminator with trainable parameters θ'

Require: $S_{\theta''}$: Discriminator with trainable parameters θ''

Require: $Dataset_L(I, M)$: Collection of labeled samples

Require: $Dataset_{UL}(I, M)$: Collection of unlabeled samples

Require: T : total number of iterations

for $t = 1, \dots, T$ **do**

Sample $I_L, M \sim Dataset_L(I, M)$

$\widehat{I}_L = G_{\theta}(I_L)$

$\widehat{M}_L = S_{\theta''}(\widehat{I}_L)$

$L_G = \lambda_{seg} L_{Dice}(\widehat{M}_L, M) + \lambda_{L1} L1(\widehat{I}_L, I_L)$

Update θ based on L_G

$M_L = S_{\theta''}(I_L)$

$L_S = (L_{Dice}(M_L, M), L_{Dice}(\widehat{M}_L, M))/2$

Update θ'' based on L_S

Sample $I_{UL} \sim Dataset_{UL}(I, M)$

$\widehat{I}_{UL} = G_{\theta}(I_{UL})$

$P_L = D_{\theta'}(I_{UL})$

$\widehat{P}_L = D_{\theta'}(\widehat{I}_{UL})$

$L_D = (L_{MSE}(P_L, 1) + L_{MSE}(\widehat{P}_L, 0))/2$ // 1:Real, 0: Fake

Update θ' based on L_D

$\widehat{M}_{UL} = S_{\theta''}(\widehat{I}_{UL})$

$$L_G = \lambda_{adv} L_{MSE}(\widehat{P}_L, 1) + \lambda_{cus} L_{customize}(\widehat{M}_{UL}) + \lambda_{L1} L1(\widehat{I}_{UL}, I_{UL}) // 1: \text{Real}, 0: \text{Fake}$$

Update θ based on L_G
 $M_{UL} = S_{\theta''}(I_{UL})$
 $L_S = (L_{customize}(\widehat{M}_{UL}) + L_{customize}(M_{UL}))/2$
Update θ'' based on L_S
end for
return $\theta, \theta', \theta''$

2) Dynamic Generator Augmentation (DGA) and Segmentation Guided Enhancement (SGE)

Traditional GAN-based augmentation methods involve pre-training the generator to create a fixed reconstructed dataset, which is then used for segmentation model training. In contrast, the proposed GRN integrates both the generator and the segmentor within a single training framework, allowing the generator G_θ to update its weight dynamically in each training iteration. An example formula for updating the generator weights at training iteration t is shown below:

$$\theta_{t+1} \leftarrow \theta_t - \eta \cdot \nabla_{\theta_t} L_G \quad (10)$$

where η is the learning rate, and ∇_{θ_t} is the gradient calculated at training iteration t . Even when the generator G_θ receives the same image I , the $G_{\theta_{t+1}}(I) \neq G_{\theta_t}(I)$ due to continuous updates of the hyperparameter θ for each epoch. This method enables the generator to produce progressively varied images from the original input images. By dynamically generating images, the segmentation model is trained on an almost limitless number of image variations. As a result, we refer to this approach as Dynamic generator augmentation (**DGA**) in this study.

In the GRN framework, the objective function is defined as $\min_G \min_S L_{Seg}(S(G(x)), y)$, where the generator G and the segmentor S share the same goal to minimize the segmentor loss. Consequently, during the inference phase, the generator and the segmentor can be integrated to provide a joint prediction $y = S(G(x))$. This two-step process, termed Segmentation Guided Enhancement (**SGE**), ensures that image enhancements are designed to improve segmentation outcomes.

C. Interpolation Consistency Loss

Similar to a previous study [32], we adopt interpolation consistency loss as our customized loss for GRN-SSL. For each image in the unlabeled batch B_{UL} , we randomly sample a second image from the same batch. Both images are processed by the generator G and segmentor S to produce their respective segmentation masks. We then randomly generate an interpolation coefficient λ from a predefined distribution to create a mixed image through an interpolation of the original and sampled images. This mixed image is subsequently processed by the generator and segmentor to obtain a corresponding segmentation mask. The interpolation consistency loss quantifies the alignment between the segmentation mask of the mixed image and the interpolated masks of the original and sampled images.

$$L_{ICT} = MSE(M_{mixed}, Mix_\lambda(M_{UL}, M_S)) \quad (11)$$

where M_{mixed} denotes the predicted mask derived from the mixed image. M_{UL} and M_S are the mask predictions based on the unlabeled image and randomly sampled image, respectively. $Mix_\lambda()$ performs the interpolation of two images based on $Mix_\lambda(Tensor_a, Tensor_b) = \lambda Tensor_a + (1 - \lambda) Tensor_b$.

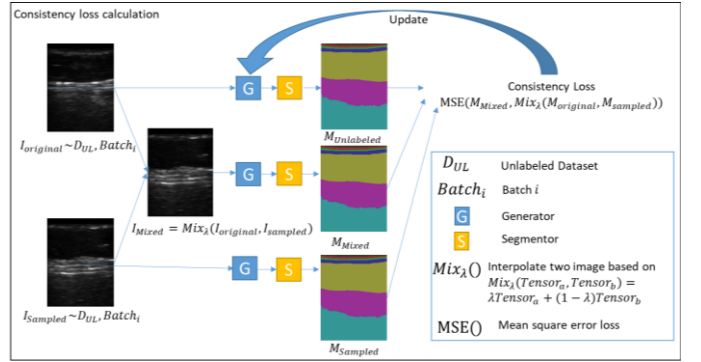


Fig. 4. Interpolation Consistency Loss Calculation. I_{UL} represents the unlabeled image, and I_S denotes a randomly sampled image from the same batch. The interpolation consistency loss enforces the model to ensure that the predicted mask from the mixed image I_M closely aligns with the interpolated mask derived from the unlabeled image I_{UL} and the randomly sampled image I_S .

D. Backbone Network Architecture

The backbone segmentation network utilizes a 2D Unet model configured with encoder channels of (16, 32, 64, 128, 256). The model is designed to accept single-channel input and produce segmentation masks for 7 classes, making it well-suited for our ultrasound imaging segmentation task. The generator encoder, illustrated in the upper section of Fig 5, incorporates residual blocks to improve gradient flow efficiency and facilitate the training of deeper network layers. The encoding process begins with an initial convolution layer that reduces spatial dimensions while increasing feature depth. This is followed by a series of residual blocks that downsample the input data. In contrast, the decoder utilizes 2D transposed convolutions to upscale high-dimensional feature representations, effectively reconstructing the images. Similar to the pix2pix model [33], we utilize a PatchGAN discriminator to assess the realism of generated images at the patch level [33]. The discriminator architecture comprises several convolution layers that progressively extract features from the input images. The discriminator outputs a patch-wise label map that evaluates the authenticity of each patch on the image.

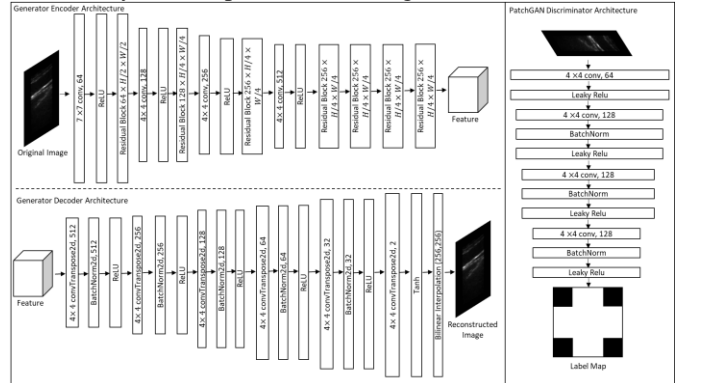


Fig. 5. Backbone network architecture. The encoder (upper section, left) utilizes multiple residual blocks to progressively capture high-dimensional patterns. The decoder (lower section, left) reconstructs the images from these high-level representations using transposed convolution layers, facilitating the accurate generation of segmentation masks.

E. Model Training and Performance Evaluation

In line with standard practices in semi-supervised learning and sample-efficient learning, we designated 5%, 10%, and 20% of

the training dataset at the patient level as labeled subsets, with the remaining data serving as unlabeled subset, for an initial comparison of GRN methods against existing approaches. We compared the performance of GRN variants (Table II) with that seven other semi-supervised learning methods, including MT[22], UAMT [23], Uncertainty Rectified Pyramid Consistency (URPC) [34], Shape-aware Semi-supervised network (SASSNet) [35], Regularized dropout (R-drop) [36], Interpolation Consistency Training (ICT) [32], and Deep Adversarial Network (DAN) [37]. All semi-supervised learning methods, including our GRN variants (Table II) and seven other comparison methods, utilized the UNet model as their backbone network.

To benchmark the GRN methods against a fully supervised setting, where the model is trained on all labeled images, we allocated 30%, 40%, 50%, and 100% of the training dataset as labeled for comparison. This approach allows the evaluation of the effectiveness of GRN methods in reducing the need for extensive image annotation while maintaining and even enhancing segmentation performance.

We further analyzed the effect of DGA, SGE, and SSL on model performance across varying proportions of labeled images for training. The effect of **DGA** was assessed by calculating the difference in dice similarity coefficient (DSC) between the **GRN-SEL** method and the fully supervised model. The effect of **SGE effect** was determined by comparing GRN variants with and without SGE, while the effect of **SSL** was evaluated by measuring the performance difference with or without the inclusion of unlabeled data for unsupervised training. Additionally, we conducted an ablation study on a 5% labeled dataset to evaluate the GRN model performance.

In training the GRN-SEL, λ_{adv} , λ_{seg} and λ_{L1} in L_G are set to 1, 100, 100, respectively. For GRN-SSL training, λ_{seg} and λ_{L1} are both set to 100. In the unsupervised training of GRN-SSL, λ_{adv} , $\lambda_{customize}$ and λ_{L1} are set to be 1, 1, 100., respectively. Following the approach of the pix2pix model [33], a smaller weight was assigned to the adversarial loss. The Adam optimizer was used for training the generator, segmentor, and discriminator, with an initial learning rate of 0.0002 and exponential decay rates β set to be (0.5, 0.999). The maximum number of epochs was set to 50. The model with the lowest dice loss on the validation dataset was selected. An early stop mechanism was implemented, terminating the training if validation performance did not improve for five consecutive epochs. The performance of the segmentation model was evaluated based on the DSC on the independent test sets, with a higher DSC indicating a greater overlap between the predicted mask and the ground truth mask. In this study, all methods were implemented using PyTorch = 2.3.1 on an NVIDIA GTX3090 GPU.

III. RESULTS

A. Performance Evaluation and Comparison

Table II presents the segmentation performance of our proposed GRN methods compared to existing techniques on the independent test set with varying proportions of labeled data (5%, 10%, 20%) involved in the training. Across all labeled data proportions, the GRN-SSL variant and GRN-SEL with

SGE consistently outperformed other methods. When trained on 5% labeled data, GRN-SEL achieved superior results compared to 5 out of 7 models without utilizing unlabeled images. At the 10% labeled level, GRN-SSL (w SGE) is only 3.46% lower than the fully supervised model trained on all labeled data. At the 20% labeled level, GRN-SSL with SGE achieved an 80.05% DSC, which is just 0.57% lower than the fully supervised model (80.62%); however, this difference is still statistically significant ($p < 0.05$).

Table III summarizes the mean DSC for each tissue layer as well as the overall mean when trained on 5% of the labeled images in the training set. The GRN-SSL variant with SGE outperformed all other methods in 3 out of 6 tissue layers significantly, while GRN-SSL exceeded the performance of other methods in 2 out of 6 layers. Although the overall DSC for GRN-SEL with SGE was higher, it did not achieve a statistically significant improvement in the segmentation of individual layers. Some examples in Fig. 7 show the prediction results of the GRN methods and other models.

Table II

COMPARISON OF SEGMENTATION PERFORMANCE BETWEEN OUR METHODS AND EXISTING METHODS IN TERMS OF DICE COEFFICIENT (95% CONFIDENCE INTERVAL)

Method	Labeled %		
	5%	10%	20%
Fully supervised	43.97 (43.71, 44.23)	64.87 (64.57, 65.17)	74.52 (74.23, 74.81)
MT[22]	65.09 (64.78, 65.40)	72.78 (72.47, 73.09)	76.82 (76.57, 77.07)
UAMT[23]	64.39 (64.04, 64.74)	72.75 (72.42, 73.08)	76.95 (76.69, 77.21)
URPC[34]	56.46 (56.17, 56.75)	73.62 (73.43, 73.81)	76.94 (76.76, 77.12)
SASSNet[35]	52.66 (52.38, 52.94)	67.27 (67.02, 67.52)	76.49 (76.29, 76.69)
R-drop[36]	65.92 (65.57, 66.27)	75.34 (75.08, 75.60)	77.35 (76.99, 77.71)
ICT[32]	66.07 (65.75, 66.39)	74.06 (73.81, 74.31)	76.54 (76.32, 76.76)
DAN[37]	64.56 (64.30, 64.82)	73.00 (72.73, 73.27)	74.34 (74.08, 74.60)
GRN-SEL	65.16 (64.82, 65.50)	73.08 (72.80, 73.36)	75.72 (75.45, 75.99)
GRN-SEL (w SGE)	66.55 (66.21, 66.89)	76.98 (76.72, 77.24)	78.85 (78.60, 79.10)
GRN-SSL	67.33 (67.03, 67.63)	75.65 (75.37, 75.93)	77.61 (77.27, 77.95)
GRN-SSL (w SGE)	68.90 (68.62, 69.18)	77.16 (76.86, 77.46)	80.05 (79.81, 80.29)

Bold denotes the proposed methods that significantly outperform all other methods ($p < 0.05$, paired t-test).

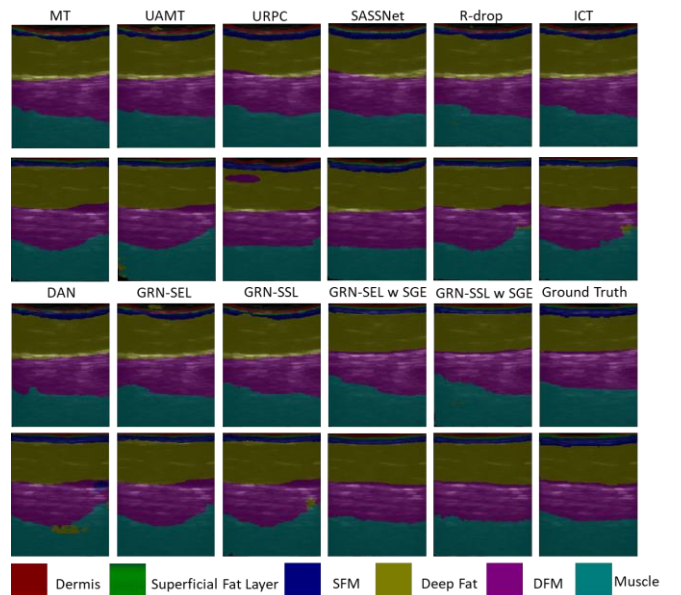


Fig. 7. Mask predictions for GRN methods and other methods when trained on the 5% labeled images in the training set. GRN variants, particularly those utilizing SGE, demonstrate superior segmentation performance and higher accuracy in tissue layer segmentation.

B. Segmentation Performance across Varying Proportions of Labeled Dataset

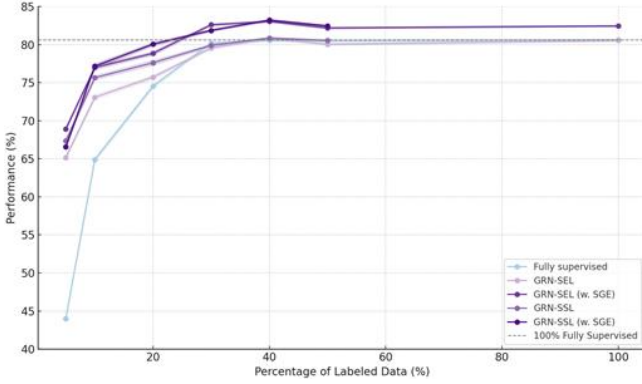


Fig. 8. Segmentation performance of GRN variants relative to the proportion of the labeled images in the training set. The dotted line indicates the performance of the models trained on all labeled images.

Table IV presents the segmentation performance of GRN variants on varying proportions of labeled images in the training set. The results indicate that with just 30% of the labeled images, the GRN-SEL with SGE achieved performance comparable to the model trained on 100% of the labeled images. Additionally, when utilizing 30% of the labeled dataset, the GRN-SSL with SGE attained performance statistically similar to the model trained on all labeled images. As the labeled image proportion increases to 40%, the GRN-SSL model matched the performance of the fully supervised approach. Even without utilizing the unlabeled dataset, the GRN-SEL achieved performance similar to those of the supervised model. Notably, the GRN framework not only maintained equivalence with fully supervised models under reduced labeling conditions but also exceeded their performance limits. Specifically, the GRN-SSL with SGE achieved a Dice coefficient that was 2.59% higher than that of the fully supervised model while utilizing only 40% of the labeled images in the training set. These findings suggest the efficacy of the GRN methods in enhancing segmentation performance while significantly reducing the need for extensive data labeling.

C. GRN Component Evaluation

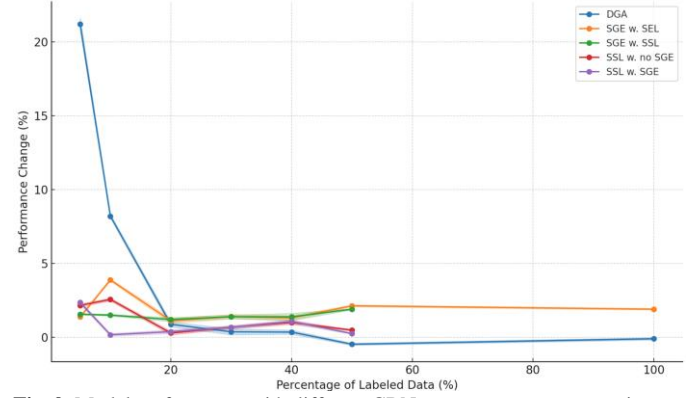


Fig. 9. Model performance with different GRN components across varying percentages of labeled images. The DGA component significantly enhances performance at lower percentages of data images but shows a diminishing effect as more labeled data is incorporated. In contrast, SSL consistently shows a strong positive impact across most data proportions.

Table V presents the individual and combined effects of DGA, SGE, and SSL on model performance across different proportions (5%, 10%, 20%, 30%, 40%, 50%, and 100%) of labeled images in the training set. The results indicate that DGA has a substantial positive impact on model performance, particularly when the labeled data is scarce. Specifically, at lower labeling proportions (5% and 10%), DGA contributes to substantial performance gains of +21.19% and +8.21%, respectively. However, its positive impact diminishes as the number of labeled images increases, with the effect dropping to -0.09% when all labeled images are used. In contrast, SGE consistently enhanced model performance across all proportions of labeled images, showing stable and robust improvements. The inclusion of SGE leads to positive effects ranging from +1.13% at 20% labeled images to +3.89% at 10% for GRN-SEL method, demonstrating its effectiveness regardless of the amount of labeled images available. A similar trend was observed with SSL: whether or not SGE is used, incorporating unlabeled data consistently improves model performance.

Table III

COMPARISON OF SEGMENTATION PERFORMANCE FOR EACH TISSUE LAYER AMONG GRN METHODS AND OTHER MODELS TRAINED ON THE 5% LABELED IMAGES IN THE TRAINING DATASET, EXPRESSED IN TERMS OF DICE COEFFICIENT (95% CONFIDENCE INTERVAL)

Methods	Dermis	Superficial Fat Layer	SFM	Deep Fat	DFM	Muscle	Overall
Fully supervised	7.06 (6.87, 7.25)	0.67 (0.64, 0.70)	57.69 (57.39, 57.99)	63.76 (63.01, 64.51)	65.78 (65.34, 66.22)	68.89 (68.57, 69.21)	43.97 (43.71, 44.23)
MT	62.98 (62.66, 63.30)	59.81 (59.40, 60.22)	69.45 (69.06, 69.84)	62.41 (61.67, 63.15)	66.40 (65.98, 66.82)	69.49 (69.14, 69.84)	65.09 (64.78, 65.40)
UAMT	60.18 (59.80, 60.56)	52.43 (51.93, 52.93)	71.09 (70.63, 71.55)	63.06 (62.31, 63.81)	69.14 (68.71, 69.57)	70.44 (70.10, 70.78)	64.39 (64.04, 64.74)
URPC	46.78 (46.14, 47.42)	18.71 (18.33, 19.09)	64.96 (64.35, 65.57)	66.90 (66.11, 67.69)	67.03 (66.59, 67.47)	74.36 (73.97, 74.75)	56.46 (56.17, 56.75)

SASSNet	34.33 (33.69, 34.97)	27.29 (26.68, 27.90)	58.28 (57.75, 58.81)	68.30 (67.54, 69.06)	60.13 (59.65, 60.61)	67.62 (67.31, 67.93)	52.66 (52.38, 52.94)
R-drop	65.05 (64.75, 65.35)	55.16 (54.65, 55.67)	68.70 (68.30, 69.10)	67.18 (66.46, 67.90)	66.65 (66.22, 67.08)	72.32 (72.02, 72.62)	65.92 (65.59, 66.25)
ICT	65.91 (65.63, 66.19)	55.44 (54.97, 55.91)	70.25 (69.83, 70.67)	64.40 (63.69, 65.11)	68.68 (68.26, 69.10)	71.75 (71.47, 72.03)	66.07 (65.75, 66.39)
DAN	62.59 (62.30, 62.88)	46.79 (46.45, 47.13)	73.93 (73.68, 74.18)	63.77 (63.09, 64.45)	67.95 (67.50, 68.40)	72.35 (72.08, 72.62)	64.56 (64.30, 64.82)
GRN-SEL	63.58 (63.20, 63.96)	54.87 (54.39, 55.35)	69.83 (69.44, 70.22)	63.90 (63.17, 64.63)	68.28 (67.85, 68.71)	70.47 (70.04, 70.90)	65.16 (64.82, 65.50)
GRN-SEL (w SGE)	65.15 (64.76, 65.54)	56.73 (56.25, 57.21)	71.23 (70.82, 71.64)	65.83 (65.06, 66.60)	68.61 (68.16, 69.06)	71.70 (71.37, 72.03)	66.55 (66.21, 66.89)
GRN-SSL	67.06 (66.77, 67.35)	58.88 (58.46, 59.30)	68.85 (68.41, 69.29)	67.46 (66.76, 68.16)	67.14 (66.73, 67.55)	74.57 (74.16, 74.98)	67.33 (67.03, 67.63)
GRN-SSL (w SGE)	69.40 (69.11, 69.69)	61.91 (61.53, 62.29)	72.11 (71.69, 72.53)	68.15 (67.44, 68.86)	67.17 (66.80, 67.54)	74.63 (74.35, 74.91)	68.90 (68.62, 69.18)

Bold text denotes the proposed methods that statistically outperform all other methods. ($p < 0.05$, paired t-test).

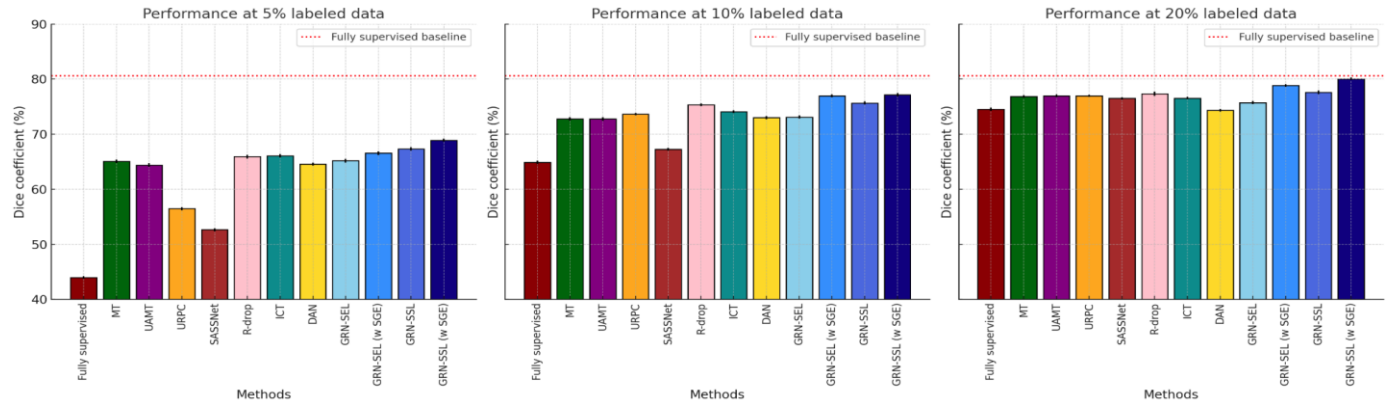


Fig. 6. Comparison of segmentation model performance across various methods trained on different amounts of labeled data (5%, 10%, and 20%). The red dotted line indicates the performance of the model when trained on 100% labeled images in the training set. The small bars on each column indicate the confidence intervals (CI) for the segmentation results of each method.

Table IV

SEGMENTATION PERFORMANCE OF THE PROPOSED GRN METHODS ON THE INDEPENDENT TEST SET WHEN TRAINING ON VARYING PROPORTIONS OF LABELED IMAGES IN THE TRAINING SET. EXPRESSED IN TERMS OF DICE COEFFICIENT (95% CONFIDENCE INTERVAL)

Method	5%	10%	20%	30%	40%	50%	100%
Fully supervised	43.97 (43.71, 44.23)	64.87 (64.57, 65.17)	74.52 (74.23, 74.81)	80.21 (80.04, 80.38)	80.53 (80.36, 80.70)	80.49 (80.33, 80.65)	80.62 (80.47, 80.77)
GRN-SEL	65.16 (64.82, 65.50)	73.08 (72.80, 73.36)	75.72 (75.45, 75.99)	79.55 (79.38, 79.72)	80.79 (80.64, 80.94)	80.04 (79.90, 80.18)	80.53 (80.39, 80.67)
GRN-SEL (w. SGE)	66.55 (66.21, 66.89)	76.98 (76.72, 77.24)	78.85 (78.60, 79.10)	82.60 (82.45, 82.75)	83.04 (82.90, 83.18)	82.18 (82.04, 82.32)	82.45 (82.33, 82.57)
GRN-SSL	67.33 (67.03, 67.63)	75.65 (75.37, 75.93)	77.61 (77.27, 77.95)	79.90 (79.73, 80.07)	80.85 (80.70, 81.00)	80.53 (80.39, 80.67)	-
GRN-SSL (w. SGE)	68.90 (68.62, 69.18)	77.16 (76.86, 77.46)	80.05 (79.81, 80.29)	81.86 (81.70, 82.02)	83.21 (83.07, 83.35)	82.45 (82.32, 82.58)	-

Bold text denotes the proposed methods statistically not inferior to 100% fully supervised model. ($p < 0.05$, paired t-test).

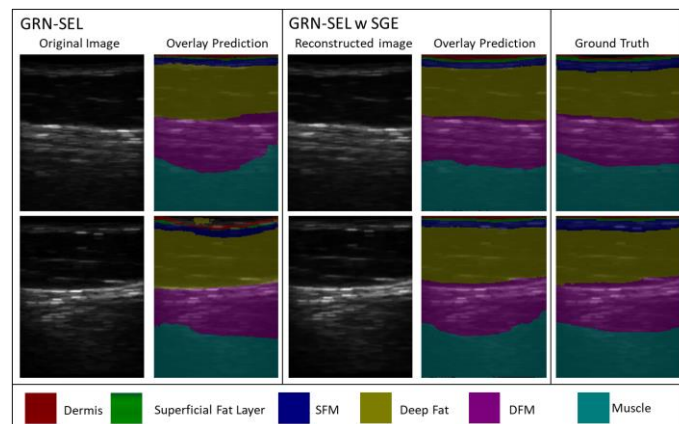
Table V

EFFECT OF DGA, SGE, AND SSL ON SEGMENTATION PERFORMANCE GAINS ACROSS VARIOUS PROPORTIONS OF LABELED IMAGES IN THE TRAINING SET, EXPRESSED IN TERMS OF DICE COEFFICIENT (95% CONFIDENCE INTERVAL)

Variable	5%	10%	20%	30%	40%	50%	100%
DGA	+21.19(+20.76, +21.62)	+8.21 (+8.09, +8.33)	+0.89 (+0.72, +1.06)	+0.38 (+0.18, +0.58)	+0.36 (+0.22, +0.50)	-0.46 (-0.53, -0.39)	-0.09 (-0.17, -0.01)
SGE w. SEL	+1.39 (+1.32, +1.46)	+3.89 (+3.81, +3.97)	+1.13 (+0.96, +1.30)	+1.41 (+1.26, +1.56)	+1.32 (+1.17, +1.47)	+2.14 (+2.08, +2.20)	+1.91 (+1.86, +1.96)
SGE w. SSL	+1.57 (+1.52, +1.62)	+1.51 (+1.45, +1.57)	+1.21 (+1.08, +1.34)	+1.40 (+1.28, +1.52)	+1.39 (+1.15, +1.63)	+1.91 (+1.86, +1.96)	-
SSL w. no SGE	+2.17 (+2.07, +2.27)	+2.57 (+2.47, +2.67)	+0.30 (+0.17, +0.43)	+0.69 (+0.59, +0.79)	+1.01 (+0.88, +1.14)	+0.49 (+0.44, +0.54)	-
SSL w. SGE	+2.36 (+2.24, +2.48)	+0.18 (+0.09, +0.27)	+0.39 (+0.27, +0.51)	+0.68 (+0.58, +0.78)	+1.08 (+0.96, +1.20)	+0.26 (+0.21, +0.31)	-

Bold text denotes the proposed methods that statistically decrease the model performance. ($CI_{bounds} < 0$, $p < 0.05$, paired t-test)

Fig. 10. Comparison of non-enhanced and enhanced images with corresponding mask prediction. The segmentation models achieve higher accuracy when utilizing SGE.



D. Ablation Study

Table VI presents the results of the ablation study on the GRN framework. The findings indicate that neither standard image augmentation nor traditional GAN augmentation methods achieved a DSC as high as GRN-SEL with DGA. The inclusion of SGE yielded a marginal increase of 0.18%. The removal of L_{seg} feedback from GRN-SEL led to a significant 5.76% decrease in DSC. The negated L_{seg} feedback further significantly degrades the segmentor's performance. Additionally, freezing the segmentor weights during the backpropagation of the generator loss L_G caused a further 8.56% decline in DSC. Conversely, implementing interpolation

consistency loss with unlabeled data in unsupervised training resulted in the greatest improvement, increasing DSC by 25.08%.

Table VI

RESULTS OF THE ABLATION STUDY EVALUATING THE PROPOSED GRN FRAMEWORK ON THE VALIDATION DATASET WHEN 5% OF IMAGES BEING LABELED

Method	DSC (%)	Improvement (%)
Fully Supervised	40.02 (39.49, 40.55)	-
Fully Supervised (w. image augmentation)	38.15 (37.78, 38.52)	-1.87
Fully Supervised (w. GAN augmentation)	53.82 (53.11, 54.53)	+13.80
GRN-SEL	57.12 (56.19, 58.05)	+17.10
GRN-SEL (w. SGE)	57.30 (56.44, 58.16)	+17.28
GRN-SEL (w/o L_{seg} feedback)	51.36 (50.38, 52.34)	+11.34
GRN-SEL (w. $-L_{seg}$ feedback)	32.74 (32.14, 33.34)	-7.28
GRN-SEL (Freeze S for back-propagate L_G)	48.56 (47.45, 49.67)	+8.54
GRN-SSL (w. SGE)	65.10 (64.35, 65.85)	+25.08

Segmentation performance is presented as percentage \pm half of CI. Segmentation performance is calculated excluding the background class. Image augmentation includes geometric augmentation and intensity augmentation. GAN augmentation indicates train GAN model for reconstructed purposes and implement the pre-trained generator to generate joint dataset ($D_{original}, D_{reconstructed}$) for the segmentor to trained with. L_{seg} feedback indicates including segmentation loss L_{seg} term in generator loss L_G . “ $-L_{seg}$ feedback” indicates that the segmentor loss is negated, causing the generator to be optimized to maximize the segmentor’s loss.

IV. DISCUSSION

We developed and validated a novel method called GRN, which synergistically integrates the joint training of a generator and a segmentor to accurately segment tissue layers depicted on B-model ultrasound imaging while significantly reducing the need for extensive image annotations. Unlike traditional unconstrained GAN-based data augmentation methods, our GRN framework features a feedback mechanism in which the segmentation model provides feedback loss to the generator, thereby guiding the image generation process to produce denoised segmentation-optimized images. Our results demonstrate that GRN-SSL with SGE can reduce data labeling efforts by up to 70% (Table IV). Meanwhile, GRN-SSL alone achieves a 60% reduction, GRN-SEL with SGE also reduces data labeling efforts by 70%, and GRN-SEL alone reduces by 60%, all while maintaining performance comparable to fully supervised models. Notably, GRN-SSL with SGE outperforms models trained on all labeled images, achieving a 2.59% higher DSC with only 40% of the labeled images in the training set. These findings suggest the effectiveness of the GRN framework in optimizing segmentation performance with significantly less labeled data, offering a scalable and efficient solution for medical image analysis while alleviating the burdens associated with data annotation.

The GRN framework offers several advantages. First, the generator continuously updates its weights, providing the segmentor with dynamically augmented images across different epochs. This process substantially increases the diversity of input data and finally improves the robustness of the model. Second, the generator serves as an optional image enhancement tool, specifically optimized to generate images that minimize the segmentor’s loss, thereby further enhancing

segmentation performance. Third, the GRN framework exhibits significant versatility. Based on the GRN-SEL, the Dice loss used to measure the performance of the segmentor could be replaced by other loss functions, such as interpolation consistency loss for GRN-SSL or rectified pyramid consistent loss in the URPC model [32, 34]. Lastly, unlike other semi-supervised learning approaches that typically require a large set of unlabeled images, GRN-SEL only relies on a small set of annotated data and supports semi-supervised learning without special requirements for the quantity of unlabeled images.

Contrary to the prevailing belief that augmentation should generate challenging and diverse datasets to enhance model performance [20], our ablation study results demonstrate that using a less diverse, denoised augmented dataset can improve model performance (Table VI). This is because training on a denoised dataset allows the model to focus on informative features. Consider a sample with two feature components ($X_{informative}, X_{noise}$), and corresponding weight matrices ($W_{informative}, W_{noise}$), the extracted feature can be expressed as: $F = W_{informative} \times X_{informative} + W_{noise} \times X_{noise}$. If the noise features are set to 0, the gradient can be expressed as:

$$\frac{\partial L}{\partial W_{noise}} = \frac{\partial L}{\partial F} \times \frac{\partial F}{\partial W_{noise}} = \frac{\partial L}{\partial F} \times X_{noise} = 0 \quad \text{when } X_{noise} = 0 \quad (12)$$

In this scenario, the weights associated with noise features W_{noise} are not updated and remain near their initial values, close to zero. This enables the model to ignore noise features and concentrate on the informative parts of the data, thereby improving overall performance.

We did not freeze segmentor weights during the backpropagation of the generator loss L_G . Although GRN shares a feedback mechanism similar to GANs by allowing the generator to receive guidance, the role of the discriminator and segmentor diverse in GRN differ from those in conventional GAN architectures. In GRN, the objective function is $\min_G (\min_S L_{seg}(S(G(x)), y))$, where the generator G and segmentor S work together to minimize the segmentation loss. Additionally, during the inference stage, the generator can serve as an image enhancement module, preprocessing input images before they enter the segmentor. Therefore, we opted not to freeze the segmentor weights. This design allows both the generator G and segmentor S to adapt dynamically with each training iteration.

The component analysis showed that the DGA significantly improves model performance when the proportion of labeled data is low; however, its impact diminishes as the amount of labeled data in the training set increases (Table V). One explanation is when dataset diversity is limited, even a small amount of augmentation can substantially increase diversity and thereby improve model performance. As the labeled data becomes more abundant, each additional augmentation contributes less to diversity, leading to diminishing returns and a plateau in performance gains. In contrast, SGE consistently enhances model performance across all levels of labeled data, including scenarios with a fully labeled dataset. This finding suggests that beyond optimizing the encoder and decoder architectures for improved performance, incorporating a

pre-enhancement model specifically tuned to minimize output loss is a vital strategy for improving model efficacy.

Our study has limitations. First, the dataset size is small due to the slow progress of patient recruitment and ongoing data collection. This limitation motivates us to develop novel solutions that minimize the need for a large dataset without spending significant time on manual annotations. To further address this concern, we set aside a relatively large independent test dataset consisting of 6430 images from 23 scans acquired on different locations of 11 subjects. Second, the DGA does not improve the model performance when more labeled images are included for training. (Table V) This may be attributed to the dataset's diversity, which is adequate for the model to learn relevant patterns, making additional augmented images less impactful on performance. Our experiments demonstrate that DGA is particularly effective when the sample size of the annotated training dataset is limited. Furthermore, the integration of SGE requires the generator to preprocess the image initially, leading to additional computational demands during the inference stage. However, SGE is an optional tool, providing users the flexibility to enhance model performance. Notably, both GRN-SEL and GRN-SSL prove their effectiveness without relying on SGE, with GRN-SSL outperforming other methods even in the absence of SGE. Despite these limitations, our experiments demonstrated the potential of the GRN in reducing the effort required for manual annotation.

V. CONCLUSION

We introduce a segmentation-aware joint training framework called GRN designed to segment tissue layers in 3-D B-mode ultrasound images. This innovative approach incorporates a segmentation loss feedback mechanism that enables the generator to produce reconstructed images specifically optimized to enhance the performance of the segmentation model. Our model achieves a higher performance compared to models trained on 100% labeled datasets, all while reducing the data labeling efforts by 60%. As a semi-supervised learning method, GRN-SEL relies on a small set of annotated data and can effectively utilize available unlabeled images, even when their quantity is limited.

REFERENCES

- [1] G. B. Andersson, "Epidemiological features of chronic low-back pain," *The lancet*, vol. 354, no. 9178, pp. 581-585, 1999.
- [2] D. G. Borenstein, "Chronic low back pain," *Rheumatic Disease Clinics*, vol. 22, no. 3, pp. 439-456, 1996.
- [3] R. D. Meucci, A. G. Fassa, and N. M. X. Faria, "Prevalence of chronic low back pain: systematic review," *Revista de saude publica*, vol. 49, p. 73, 2015.
- [4] C. G. Maher, "Effective physical treatment for chronic low back pain," *Orthopedic Clinics*, vol. 35, no. 1, pp. 57-64, 2004.
- [5] J. D. Cassidy, L. J. Carroll, and P. Côté, "The Saskatchewan health and back pain survey: the prevalence of low back pain and related disability in Saskatchewan adults," *Spine*, vol. 23, no. 17, pp. 1860-1866, 1998.
- [6] J. R. Chapman *et al.*, "Evaluating common outcomes for measuring treatment success for chronic low back pain," *Spine*, vol. 36, pp. S54-S68, 2011.
- [7] K. Yokosuka *et al.*, "Computed tomographic epidurography in patients with low back pain and leg pain: a single-center observational study," *Diagnostics*, vol. 12, no. 5, p. 1267, 2022.
- [8] M. Kamaz, D. Kiresi, H. Oguz, D. Emlik, and F. Levendoglu, "CT measurement of trunk muscle areas in patients with chronic low back pain," *Diagnostic and interventional radiology*, vol. 13, no. 3, p. 144, 2007.
- [9] L. A. Danneels, G. Vanderstraeten, D. C. Cambier, E. E. Witvrouw, H. J. De Cuyper, and L. Danneels, "CT imaging of trunk muscles in chronic low back pain patients and healthy control subjects," *European spine journal*, vol. 9, pp. 266-272, 2000.
- [10] T. M. Buzug, "Computed tomography," in *Springer handbook of medical technology*: Springer, 2011, pp. 311-342.
- [11] G. Katti, S. A. Ara, and A. Shireen, "Magnetic resonance imaging (MRI)—A review," *International journal of dental clinics*, vol. 3, no. 1, pp. 65-70, 2011.
- [12] D. Chou *et al.*, "Degenerative magnetic resonance imaging changes in patients with chronic low back pain: a systematic review," *Spine*, vol. 36, no. 21 Suppl, pp. S43-S53, 2011.
- [13] W. K. Cheung, J. P. Y. Cheung, and W.-N. Lee, "Role of ultrasound in low back pain: A review," *Ultrasound in medicine & biology*, vol. 46, no. 6, pp. 1344-1358, 2020.
- [14] B. L. Partik *et al.*, "3D versus 2D ultrasound: accuracy of volume measurement in human cadaver kidneys," *Investigative radiology*, vol. 37, no. 9, pp. 489-495, 2002.
- [15] Q. Huang and Z. Zeng, "A review on real-time 3D ultrasound imaging technology," *BioMed research international*, vol. 2017, no. 1, p. 6027029, 2017.
- [16] A. Parnami and M. Lee, "Learning from few examples: A summary of approaches to few-shot learning," *arXiv preprint arXiv:2203.04291*, 2022.
- [17] K. Han *et al.*, "Deep semi-supervised learning for medical image segmentation: A review," *Expert Systems with Applications*, p. 123052, 2024.
- [18] I. Goodfellow *et al.*, "Generative adversarial networks," *Communications of the ACM*, vol. 63, no. 11, pp. 139-144, 2020.
- [19] K. Maharana, S. Mondal, and B. Nemade, "A review: Data pre-processing and data augmentation techniques," *Global Transitions Proceedings*, vol. 3, no. 1, pp. 91-99, 2022.
- [20] C. Chen *et al.*, "Enhancing MR image segmentation with realistic adversarial data augmentation," *Medical Image Analysis*, vol. 82, p. 102597, 2022.
- [21] J. Lemley, S. Bazrafkan, and P. Corcoran, "Smart augmentation learning an optimal data augmentation strategy," *Ieee Access*, vol. 5, pp. 5858-5869, 2017.
- [22] A. Tarvainen and H. Valpola, "Mean teachers are better role models: Weight-averaged consistency targets improve semi-supervised deep learning results," *Advances in neural information processing systems*, vol. 30, 2017.
- [23] L. Yu, S. Wang, X. Li, C.-W. Fu, and P.-A. Heng, "Uncertainty-aware self-ensembling model for semi-supervised 3D left atrium segmentation," in *Medical image computing and computer assisted intervention—MICCAI 2019: 22nd international conference, Shenzhen, China, October 13–17, 2019, proceedings, part II 22*, 2019: Springer, pp. 605-613.
- [24] X. Luo, J. Chen, T. Song, and G. Wang, "Semi-supervised medical image segmentation through dual-task consistency," in *Proceedings of the AAAI conference on artificial intelligence*, 2021, vol. 35, no. 10, pp. 8801-8809.
- [25] K. Wang *et al.*, "Semi-supervised medical image segmentation via a tripled-uncertainty guided mean teacher model with contrastive learning," *Medical Image Analysis*, vol. 79, p. 102447, 2022.
- [26] J. Lyu, B. Sui, C. Wang, Q. Dou, and J. Qin, "Adaptive feature aggregation based multi-task learning for uncertainty-guided semi-supervised medical image segmentation," *Expert Systems with Applications*, vol. 232, p. 120836, 2023.
- [27] M. Frid-Adar, I. Diamant, E. Klang, M. Amitai, J. Goldberger, and H. Greenspan, "GAN-based Synthetic Medical Image Augmentation for increased CNN Performance in Liver Lesion Classification," *arXiv e-prints*, p. arXiv: 1803.01229, 2018.
- [28] G. Mariani, F. Scheidegger, R. Istrate, C. Bekas, and C. Malossi, "BAGAN: Data Augmentation with Balancing GAN," in *International Conference on Machine Learning*, 2018.
- [29] B. Xu, D. Zhou, and W. Li, "Image enhancement algorithm based on GAN neural network," *IEEE Access*, vol. 10, pp. 36766-36777, 2022.

- [30] Y. Ma *et al.*, "Structure and illumination constrained GAN for medical image enhancement," *IEEE Transactions on Medical Imaging*, vol. 40, no. 12, pp. 3955-3967, 2021.
- [31] A. Bissoto, E. Valle, and S. Avila, "Gan-based data augmentation and anonymization for skin-lesion analysis: A critical review," in *Proceedings of the IEEE/CVF conference on computer vision and pattern recognition*, 2021, pp. 1847-1856.
- [32] V. Verma *et al.*, "Interpolation consistency training for semi-supervised learning," *Neural Networks*, vol. 145, pp. 90-106, 2022.
- [33] P. Isola, J.-Y. Zhu, T. Zhou, and A. A. Efros, "Image-to-image translation with conditional adversarial networks," in *Proceedings of the IEEE conference on computer vision and pattern recognition*, 2017, pp. 1125-1134.
- [34] X. Luo *et al.*, "Semi-supervised medical image segmentation via uncertainty rectified pyramid consistency," *Medical Image Analysis*, vol. 80, p. 102517, 2022.
- [35] S. Li, C. Zhang, and X. He, "Shape-aware semi-supervised 3D semantic segmentation for medical images," in *Medical Image Computing and Computer Assisted Intervention—MICCAI 2020: 23rd International Conference, Lima, Peru, October 4–8, 2020, Proceedings, Part I 23*, 2020: Springer, pp. 552-561.
- [36] L. Wu *et al.*, "R-drop: Regularized dropout for neural networks," *Advances in Neural Information Processing Systems*, vol. 34, pp. 10890-10905, 2021.
- [37] Y. Zhang, L. Yang, J. Chen, M. Fredericksen, D. P. Hughes, and D. Z. Chen, "Deep adversarial networks for biomedical image segmentation utilizing unannotated images," in *Medical Image Computing and Computer Assisted Intervention—MICCAI 2017: 20th International Conference, Quebec City, QC, Canada, September 11-13, 2017, Proceedings, Part III 20*, 2017: Springer, pp. 408-416.